Numerical analysis of impurities transport in a unidirectional solidification furnace

Gao, Bing
Research Institute for Applied Mechanics, Kyushu University

Nakano, Satoshi
Research Institute for Applied Mechanics, Kyushu University

Kakimoto, Koichi
Research Institute for Applied Mechanics, Kyushu University

Numerical analysis of impurities transport in a unidirectional solidification furnace

Bing Gao*, Satoshi Nakano*, Koichi Kakimoto*

E-mail of corresponding author:*gaobing@riam.kyushu-u.ac.jp*

(Received July 31, 2009)

Abstract

For accurate prediction of carbon and oxygen impurities in multicrystalline silicon material for solar cells, global simulation of coupled oxygen and carbon transport in a unidirectional solidification furnace was implemented. Both the gas flow and silicon melt flow were considered. Five chemical reactions were included during the transportation of impurities. The simulation results show good agreement with experimental data. The effect of flow rate on impurities was examined. An increase in flow rate can reduce both carbon and oxygen impurities in the crystal, though the reduction of carbon is more obvious.

Key words : *Global simulation; unidirectional solidification furnace; solar cells; carbon and oxygen impurities; gas flow and silicon melt flow; effect of flow rate.*

1.   Introduction

Multicrystalline silicon has now become the main material in the photovoltaic market because of its low production cost and because of the high conversion efficiency of made from this material. The unidirectional solidification method is a cost-effective technique for large-scale production of multicrystalline silicon material. Similar to the Czochralski method for crystal growth, the unidirectional solidification method is also related to transport of impurities [1]. The main impurities in the crystal are oxygen and carbon. Effective control of oxygen and carbon concentrations in a crystal is required for the production of a high-quality crystal. Experimental exploration [2-4] has been carried out, but many limitations such as time, cost and complexity for analysis. Developments in computer technology have made it possible to simulate the global environments of crystal growth and find techniques for improving the purity of crystals. Many simulations of impurity transport have been done [5-15]; however, most of them were local simulations [5-11] that neglected gas transport of impurities. There have been a few studies using global simulations [12-15]. However, neglected the oxygen and carbon impurities in the silicon melt were neglected in one of those studies [12], and the carbon impurity in both gas and silicon melt was in the

other studies [13-15]. There have been no simulations that took into account not only the oxygen impurity but also the carbon impurity in both cooling gas and silicon melt. We therefore developed a set of analysis system that includes all of processes in crystal growth. This set of analysis system incorporates the silicon melt flow into the global simulation of Bornside and Brown [12]. The original boundary assumption of constant SiO concentration at the melt surface [12] is replaced by a dynamic update of SiO concentration. Therefore, this set of analysis system enables prediction of the oxygen impurity in a crystal. Another assumption of the equilibrium system in the melt [12], i.e., the carbon flux from the gas into the melt being equal to that from the melt into the crystal, is also replaced by a local nonequilibrum consideration. The carbon flux at the gas/melt interface is calculated locally and thus carbon accumulation in the melt is included. Therefore, the present simulation might be able to correct the difference between the simulation data and experimental data [12].

On the other hand, almost all of the global simulations about impurities [12-15] were based on the Czochralski method; there has been no simulation based on the unidirectional solidification method for solar cells. Therefore, a global simulation in a unidirectional solidification furnace that considers all of the processes in crystal growth is needed.

Our simulation implementation involves three steps: first, the temperature distribution of furnace components due to heat transfer and heat radiation is computed without gas flow;

*   Research Institute for Applied Mechanics, Kyushu University

second, the flow field and temperature field of the cooling argon gas are computed using the temperature boundary conditions from the first step; and third, carbon and oxygen impurities in the gas and melt are computed using the flow field and temperature field from the second step.

2. Simulation procedures

2.1 Global heat transfer

For our studies, a unidirectional solidification furnace is assumed to be axisymmetric. All of the components of the furnace are subdivided into a set of block regions, each of which is covered with a structured grid. The configurations of the furnace and its computational grids for global heat transfer are shown in Fig. 1. In Fig. 1, the crucible 3 is made of quartz; the crucible 4, the heat shields 7-11, the heaters 12-15 and the pedestal 5 are made of carbon; the pedestal 6 are made of steel.
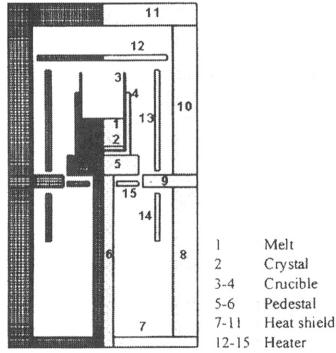
Fig. 1. Configuration of the unidirectional solidification furnace and its computational grids for global heat transfer.

Global modeling of heat transfer in the furnace involves convective heat transfer of the melt in the crucible, conductive heat transfer in all solid components and radiation heat transfer in all enclosures of the furnace. The melt flow in the crucible is assumed to be an incompressible laminar flow. The radiative heat exchange in all radiative enclosures is modeled on the basis of the assumption of diffuse-gray surface radiation. The growth system is assumed to be quasi-steady. The convective cooling by argon gas is neglected in the computation of thermal fields. For details of the global heat transfer, refer to Liu and Kakimoto [16].

2.2 Argon gas flow

The flow of argon gas through the furnace is considered to be a compressible and axisymmetric flow. Similar to the simulation of global heat transfer, the flow domain is subdivided into a set of block regions, each of which is covered with a structured grid. The radius of the inlet and width of the outlet for the simulation are 3.5 mm and 4 mm, respectively.

Full Navier-Stokes equations without any assumptions are used. The conservative compressible Navier-Stokes equations for axisymmetric geometry are described in detail in the book [17]. A second-order total variation diminishing (TVD) scheme is used for convection terms and Davis-Yee symmetric TVD is used for the flux limiter vectors [17]. An entropy correction term is also introduced to satisfy the entropy condition. A fourth-order Runge-Kutta scheme is used for time marching and a central difference scheme is used for viscous terms. Local time step [17] and low Mach number acceleration technique [18] are adopted for efficiency. The domain-decomposition method is used to solve the whole flow field.

The temperatures at all solid surfaces are set to the values computed from the global heat transfer. The velocities at all solid surfaces are set to zero. For the conditions at inlet and outlet, different methods can be used according to our practical tests. For the first simulation, inlet flow rate is set to 0.8 liter/min, inlet static temperature is set to 350K and inlet tangential velocity is set to zero. The outlet static pressure is set to 0.1 atm.

2.3 Impurity concentrations

It has been known that oxygen impurity originates from the dissolution of a silica crucible [12]. The dissolved oxygen combines with a silicon atom to form gas-phase SiO at the gas/melt interface [12]. The SiO is then carried by argon gas flow to all of the graphite components of the furnace and reacts with them to form CO [12]. The resultant CO is transported back to the melt surface by diffusion or convection [12]. Finally, the CO is dissolved into the melt and the C and O atoms are segregated into the crystal [12].

Present global simulation includes two parts: one is the calculation of SiO and CO concentrations in gas; the other is the calculation of C and O atom concentrations in melt. For the first part, refer to the paper of Bornside and Brown [12], but the original boundary assumption of constant SiO concentration at the melt surface [12] is replaced by a dynamic update of SiO concentration; for the second part, we give a detailed illumination for equations and boundary conditions.

The C and O atom concentrations in melt are assumed to be dilute in the melt and modeled as

$$\frac{\partial c_O}{\partial t} + \nabla \cdot (c_O \vec{u}_{Si}) = \nabla \cdot [c_{Si} D_O \nabla (\frac{c_O}{c_{Si}})], \qquad (1)$$

$$\frac{\partial c_C}{\partial t} + \nabla \cdot (c_C \vec{u}_{Si}) = \nabla \cdot [c_{Si} D_C \nabla (\frac{c_C}{c_{Si}})], \qquad (2)$$

where c_C is the molar concentration of carbon atoms in the melt, c_O is the molar concentration of oxygen atoms in the melt and c_{Si} is the molar concentration of silicon atoms. The vector $\vec{u}_{Si}$ is the flow vector of silicon melt. D_O and D_C are diffusivities of oxygen and carbon in the melt, respectively.

Their values are taken to be $5.0 \times 10^{-8} \ m^2/s$ [20].

From For boundary conditions of carbon on the crucible wall, zero flux is defined; for boundary conditions of oxygen on the crucible wall, a dissolution reaction is considered, that is

$$SiO_2(s) \leftrightarrow Si(m) + 2O(m).$$ (3)
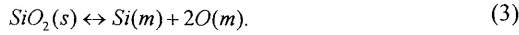
In this paper, the index symbol (s) denotes solid, (m) denotes melt, (g) denotes gas, (l) denotes liquid and (c) denotes crystal. For the present furnace, the equilibrium concentration of oxygen atoms c_O on the wall of the quartz crucible is expressed as [1]

$$c_O = \frac{b}{1-b} \times 0.5 \times 10^{23} [atom/cm^3],$$
$$b = 1.32 \times \exp\left(\frac{-7150}{T} - 6.99\right).$$ (4)

For boundary conditions of carbon and oxygen in the gas/melt interface, two chemical reactions are considered:

$$O(m) + Si(l) \leftrightarrow SiO(g),$$ (5)

$$CO(g) \leftrightarrow C(m) + O(m).$$ (6)

The equilibrium relationship between the concentration of SiO(g) and the concentration of O(m) is given in the paper [12]:

$$c_{SiO} = \frac{101325}{RT} \frac{c_O}{c_{Si}} e^{-21000/T+17.8}.$$ (7)

The equilibrium relationship between the concentration of CO(g) and the concentration of O(m) and C(m) is given as [12]

$$c_{CO} = \frac{101325}{RT} \frac{c_O}{c_{Si}} \frac{c_C}{c_{Si}} e^{-5210/T+14.5}.$$ (8)

Eqs. (7) and (8) can be regarded as boundary conditions for the gas/melt interface. Other than those, two extra boundary conditions are required for solving the four unknowns c_{SiO}, c_{CO}, c_O and c_C at that interface. We introduce the conservation of moles for carbon and oxygen. That means the flux of oxygen and carbon at that interface should satisfy the following:

For carbon:

$$c_{Ar} D_{CO} \nabla\left(\frac{c_{CO}}{c_{Ar}}\right) = c_{Si} D_C \nabla\left(\frac{c_C}{c_{Si}}\right).$$ (9)

For oxygen:

$$c_{Ar} D_{SiO} \nabla\left(\frac{c_{SiO}}{c_{Ar}}\right) + c_{Ar} D_{CO} \nabla\left(\frac{c_{CO}}{c_{Ar}}\right) = c_{Si} D_O \nabla\left(\frac{c_O}{c_{Si}}\right).$$ (10)

Eqs. (7), (8), (9) and (10) are a set of nonlinear second-order equations. The concentrations of c_{SiO}, c_{CO}, c_O and c_C at the interface can be expressed by the values of

inner field points if Eqs. (9) and (10) are discretized and substituted into Eqs. (7) and (8). However, although those concentrations can be solved directly, extremely fine grids at the melt side of interface are still required for numerical stability. As has already been known, there is a dramatic difference between the diffusivity in gas ($10^{-3} m^2/s$) and that in melt ($10^{-8} m^2/s$). The flux of O(m) and C(m) is negligible without fine grids. In the present simulation, the minimum grid in the axis direction is about 5 μm and that in the radius direction is about 0.7 mm. Fine grids require a small marching time step to keep numerical stability. We set $\Delta t = 0.001s$ for impurity calculation in both the melt and gas field.

3 Distribution of impurities

3.1 Distribution of SiO(g) in gas and O(m) in melt

The concentrations of SiO(g) and O(m) are shown in Figs. 2 and 3. The basic order of SiO(g) concentration in the gas is $10^{-9} \ mol/cm^3$ and the maximum concentration is about $10^{-8} \ mol/cm^3$, which are almost same as the simulation results of Smirnov and Kalaev [14] in a Czochralski furnace. The basic order of oxygen atom concentration in the melt is $10^{17} \ atom/cm^3$, which is consistent with the experimental result of Matsuo [1].
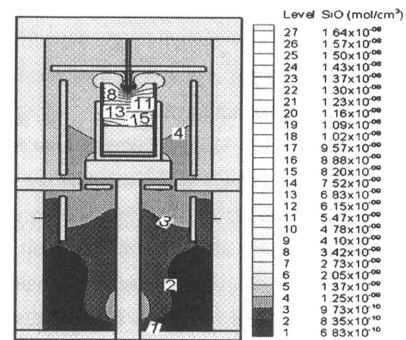
Fig. 2. SiO concentration in argon gas.

The concentration of SiO is large in the top half of the furnace and small in the bottom half of the furnace. SiO(g) evaporates from the melt surface and is carried by the gas from the top of the furnace to the bottom of the furnace. During the transportation, SiO(g) reacts with hot carbon walls and reduces gradually. Therefore, the distribution of the SiO(g) is valid if the chemical reaction is considered.

, The concentration of O(m) is small at the center of the crucible and large at the wall of the crucible. At the gas/melt interface, the concentration of O(m) is minimum. O(m) origins from the wall of the crucible and is transported to the center of the crucible by convection or diffusivity. At the gas/melt interface, O(m) combines with Si(m) to form SiO gas. Thus, the distribution of the O(m) is also consistent with

the reality.
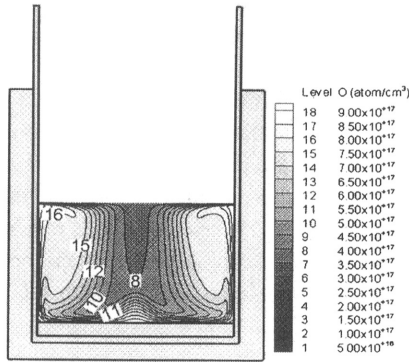
Fig. 3. Oxygen atom concentration in the melt.
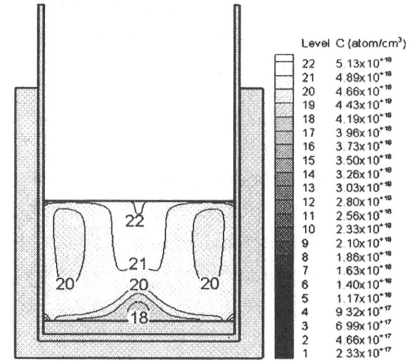
3.2 Distributions of CO(g) in gas and C(m) in melt

CO(g) in gas and C(m) in melt are shown Figs. 4 and 5. The maximum CO concentration in gas is about 10^{-9} mol/cm^3 , which is one order less than the maximum SiO concentration. The minimum CO concentration is about 10^{-10} mol/cm^3 , which lies on the melt surface. Similar to SiO(g), the concentration of CO is large in the top half of the furnace except inside the crucible and small in the bottom half of the furnace. It is understandable that CO(g) is a resultant of reaction, which is proportional to SiO(g) concentration.

The basic order of C(m) concentration is about 10^{+18} $atom/cm^3$, which is the same as the experimental result reported by Ganesh et al. [22]. The concentration of C(m) in the melt is large at the top of the melt and small at the bottom of the melt. This distribution is consistent with the process in which CO(g) is first absorbed and dissolved in the melt and then carbon is transported to the bottom by convection or diffusion.

Fig. 4. CO concentration in gas.

Fig. 5. Carbon atom concentration in the melt.
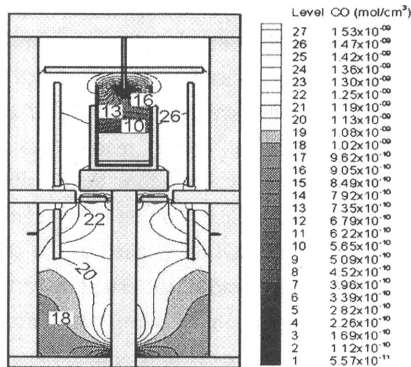
4 Comparison with experiments

Results of the simulation were compared with experimental results. Figure 5 shows that the carbon concentration at the bottom of the crucible is 4.19×10^{18} $atom/cm^3$ .After considering the segregation relation, the carbon concentration in the crystal can be expressed as

$$c_C(c) = 0.07 \times 4.19 \times 10^{18} = 3.0 \times 10^{17} atom/cm^3. \quad (11)$$

Experimental results for carbon concentration [22] at normal freezing are in the range of 2.2×10^{17} $atom/cm^3$ to 4.2×10^{17} $atom/cm^3$ .The simulated carbon concentration falls into this range of experimental data.

Figure 3 shows that the oxygen concentration at the bottom of the crucible is 5.5×10^{17} $atom/cm^3$. In a similar way, the oxygen concentration in the crystal is given by

$$c_O(c) = 0.85 \times 5.5 \times 10^{17} = 4.6 \times 10^{17} atom/cm^3. \quad (12)$$

Experiment results for oxygen concentration [23] at normal freezing are in the range of 4×10^{17} $atom/cm^3$ to 5×10^{17} $atom/cm^3$ .The simulated oxygen concentration also falls into this range of experimental data.

5 Effects of flow parameters
5.1 Flow rate effect

The effect of flow rate through the furnace on oxygen and carbon concentrations in the crystal was tested. The inlet static temperature was fixed at 350 K and the outlet static pressure was fixed at 0.1 atm . The simulations was performed with flow rates of 0.8 , 1.6 , 2.4 , 3.2 and 4.0 $liter/min$. The variations of carbon and oxygen concentrations with flow rates at a specific point are shown in Figs. 6 and 7. As the flow rate is increased by 5 fold from 0.8 $liter/min$ to 4.0 $liter/min$, the carbon concentration in the crystal decreases by 6 fold from

3.28×10^{17} $atom/cm^3$ to 0.54×10^{17} $atom/cm^3$ and the oxygen concentration decreases by 13%. Thus, an increase in flow rate can obviously reduce the carbon impurity in the crystal.
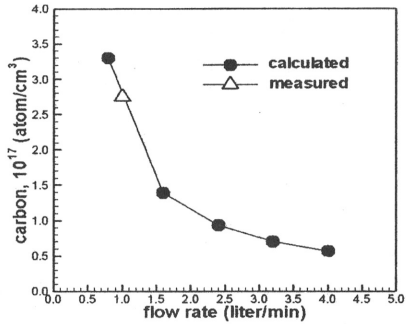
Fig. 6. Carbon atom concentration in the crystal at a pressure of 0.1 atm.
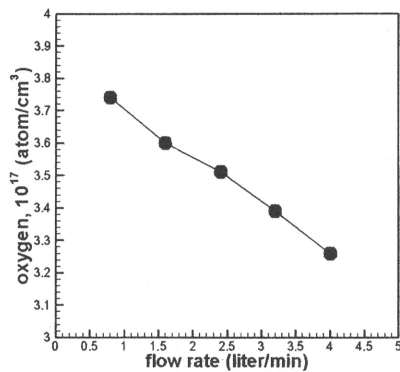
Fig. 7. Oxygen atom concentration in the crystal at a pressure of 0.1 atm.
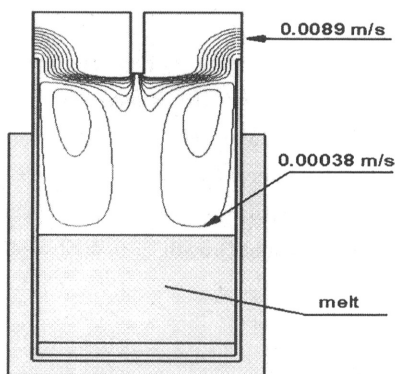
Fig. 8. Stream function of gas flow above the melt at a flow rate of 0.8 liter/min and pressure of 0.1 atm.

Stream functions above the melt at flow rates

of 0.8 *liter* / min and 4.0 *liter* / min are given in Fig. 8 and Fig. 9. When the flow rate is increased by 5 fold, the outgoing velocity of a specific point at the gap between crucible 3 and heater 12 increases by 2 fold from 0.0089 to 0.0180 m/s. That gap is an entrance of the carbon from the outside of the crucible. Therefore, it becomes more difficult for CO(g) to diffuse toward the inside of the crucible. Figures 10 and 11 show a comparison of the CO(g) concentration distributions near that gap when the flow rate is increased. It is obvious that large flow rate causes a small CO(g) concentration distribution. This effect is reflected in the large reduction of carbon concentration in the crystal as the flow rate is increased.
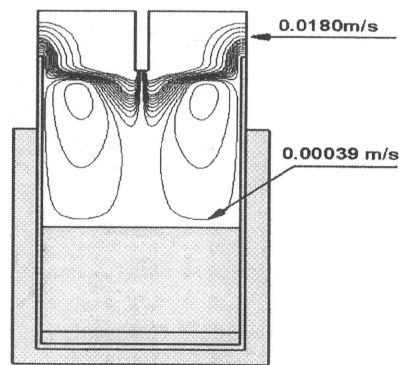
Fig. 9. Stream function of gas flow at a flow rate 4.0 liter/min and pressure of 0.1 atm.

Similarly, as the velocity at that gap increases, it becomes easier for SiO(g) to be transported toward the outside of the crucible. Thus, an increase of flow rate also reduces oxygen concentration in the crystal. However, the quantity of SiO transported by top convection flow is limited by the quantity transported by recirculation. Therefore, an increase in flow rate under the condition of pressure of 0.1 *atm* can reduce the oxygen concentration but not obviously.

6 Conclusions

Global simulation of oxygen and carbon impurities in a unidirectional solidification furnace for solar cells was implemented. Both gas transport and melt transport were included. Five chemical reactions were considered. The impurity distributions in the gas and melt were given. The present simulation results showed good agreement with experimental data. Effects of flow rate on impurities was also examined. An increase in flow rate can obviously reduce carbon impurity in the crystal; Flow rate can also affect the oxygen impurity but not obviously.
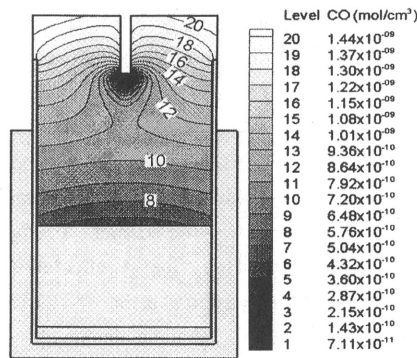
Fig. 10. Distribution of CO(g) concentration above the melt at a flow rate 0.8 liter/min and pressure of 0.1 atm.
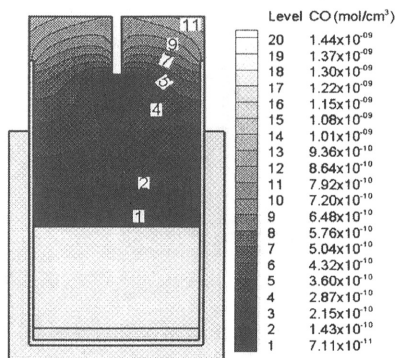
Fig. 11. Distribution of CO(g) concentration above the melt at a flow rate 4.0 liter/min and pressure of 0.1 atm.

References

1) H. Matsuo, R. B. Ganesh, S. Nakano, L. J. Liu, Y. Kangawa, K. Arafune, Y. Ohshita, M. Yamaguchi, K. Kakimoto, J. Crystal Growth, 310, 2204 (2008).

2) N. Machida, Y. Suzuki, K. Abe, N. Ono, M. Kida, Y. Shimizu, J. Crystal Growth, 186, 362 (1998).

3) N. Machida, K. Hoshikawa, Y. Shimizu, J. Crystal Growth 210, 532 (2000).

4) C. Reimann, J. Friedrich, G. Müller, S. Wurzner, H. J. Möller, 22nd European Photovoltaic Solar Energy Conference, Milan, Italy (2007).

5) N. Kobayashi, J. Crytal Growth, 108, 240 (1991).

6) H. Hirata, K. Hoshikawa, J. Crystal Growth, 125, 181 (1992).

7) T. A. Kinney, R. A. Brown, J. Crystal Growth, 132, 551 (1993).

8) K. Kakimoto, K. W. Yi, M. Eguchi, J. Crystal Growth, 163, 238 (1996).

9) K. W. Yi, K. Kakimoto, M. Eguchi, H. Noguchi, J. Crystal Growth, 165, 358 (1996).

10) M. Watanabe, K. W. Yi, T. Hibiya, K. Kakimoto, Progr. Crystal Growth Characterization Mater., 38, 215 (1999).

11) C. Reimann, T. Jung, J. Friedrich, G. Müller, Proceedings of the 33rd IEEE Photovoltaic Specialists Conference, ISBN 978-1-4244-1641-7, 2008.

12) D. E. Bornside and R. A. Brown, J. Electrochem. Soc., Vol. 142, No. 8, 2790 (1995).

13) Y. R. Li, M. W. Li, N. Imaishi, Y. Akiyama, T. Tsukada, J. Crystal Growth, 267, 466 (2004).

14) A. D. Smirnov, V. V. Kalaev, J. Crystal Growth, 310, 2970 (2008).

15) A. D. Smirnov, V. V. Kalaev, J. Crystal Growth, 311, 829 (2009).

16) L. J. Liu, K. Kakimoto, In. J. Heat Mass Transfer, 48, 4481 (2005).

17) K. A. Hoffmann, S. T. Chiang, Computational fluid dynamics. Volume II, 69 (2000).

18) P. Jenny, B. Müller, Computers & Fluids, 28, 951 (1999).

19) R. C. Reid, J. M. Prausnitz, and T. K. Sherwood, The properties of Gases and Liquids, 3rd ed., McGraw-Hill, Inc., New York (1987).

20) L. J. Liu, S. Nakano, K. Kakimoto, J. Crystal Growth, 299, 48 (2007).

21) K. Hoshikawa, X. Huang, Mater. Sci. Eng., B72, 73 (2000).

22) R. B. Ganesh, H. Matsuo, T. Kawamura, Y. Kangawa, K. Arafune, Y. Ohshita, M. Yamaguchi, K. Kakimoto, J. Crystal Growth, 310, 2697 (2008).

23) H. Matsuo, R. Bairava Ganesh, S. Nakano, L. J. Liu, Y. Kangawa, K. Arafune, Y. Ohshita, M. Yamaguchi, K. Kakimoto, J. Crystal Growth, 310, 4666 (2008).